


Model-Based Design Optimization of Underwater Flagellate Propellers

Costanza Armanini , *Member, IEEE*, Aysha Ali Alshehhi , Anup Teejo Mathew , Ikhlas Ben Hmida , Cesare Stefanini, and Federico Renda , *Associate Member, IEEE*

Abstract—A new family of soft underwater propellers has been recently presented. Mimicking the swimming strategy of bacterial flagella, these modules passively adapt to the surrounding fluid to provide a propulsive thrust. In the present paper we aim at further investigating the behaviour of this device and we address the optimization of its design towards improved swimming capabilities. This process is allowed by an accurate, yet simple, theoretical model which is able to precisely describe the robot's behaviour. The optimal prototype is fabricated, employing a composite material that is ad-hoc designed to provide the optimal stiffness. Finally, a simple robotic prototype is built and tested to validate the improved performances.

Index Terms—Modeling, control, and learning for soft robots, Soft robot applications.

I. INTRODUCTION

ONE of the most appealing property of soft robotics devices is their *embodied intelligence* [1]. This new trend in robotics aims at obtaining improved performances exploiting the adaptive behaviour of the robot when interacting with the surrounding environment [2]. The interaction is thus mostly defined by the shape of the robot and its components and by their materials. Soft robots are a great example of embodied intelligent systems, since their improved capabilities are the result of the employment of deformable, elastic, materials that can easily adapt to external stimuli [3], [4]. This is demonstrated by the large number of soft robotics devices that have been presented in the last decade, ranging in almost every possible

Manuscript received 24 February 2022; accepted 1 July 2022. Date of publication 21 July 2022; date of current version 2 August 2022. This letter was recommended for publication by Associate Editor C. Majidi and Editor C. Laschi upon evaluation of the reviewers' comments. This work was supported in part by the US Office of Naval Research Global under Grant N62909-21-1-2033 and in part by the Khalifa University of Science and Technology under Grants CIRA-2020-074 and RC1-2018-KUCARS. (*Corresponding author: Costanza Armanini.*)

Costanza Armanini, Aysha Ali Alshehhi, Anup Teejo Mathew, and Ikhlas Ben Hmida are with the Department of Mechanical Engineering, Khalifa University of Science and Technology, Abu Dhabi 127788, UAE (e-mail: costanza.armanini@ku.ac.ae; 100042463@ku.ac.ae; anup.mathew@ku.ac.ae; 100050102@ku.ac.ae).

Cesare Stefanini is with the BioRobotics Institute, Scuola Superiore Sant'Anna, 56025 Pisa, Italy (e-mail: c.stefanini@sssup.it).

Federico Renda is with the Khalifa University Center for Autonomous Robotic Systems (KUCARS), Khalifa University of Science and Technology, Abu Dhabi 127788, UAE, and also with the Department of Mechanical Engineering, Khalifa University of Science and Technology, Abu Dhabi 127788, UAE (e-mail: federico.renda@ku.ac.ae).

This letter has supplementary downloadable material available at <https://doi.org/10.1109/LRA.2022.3192886>, provided by the authors.

Digital Object Identifier 10.1109/LRA.2022.3192886

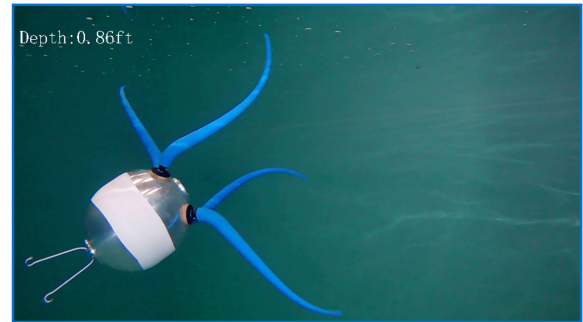


Fig. 1. Swimming of the 4-flagellated robot presented in [17].

technological field, from biomedical engineering to aerospace and, finally, underwater robotics [5]–[12]. Indeed, soft robots are characterized by a great adaptability which is mostly provided by their own body and that can be obtained using few control inputs. Having a virtually infinite number of degrees of freedom, one of the biggest challenge in designing soft robot consists in their theoretical modeling. This lead to the definition of a great number of modelling techniques, mostly varying in their reduction and discretization level [13]. On the other side, the employment of these techniques to perform model-based optimizations is still a rather unexplored field, though growing in numbers [14]–[16]. In [17] the authors presented a new family of soft, underwater modules which exploit their passive elasticity to provide a propulsive thrust, Fig. 1. Mimicking the swimming strategy adopted by bacterial flagella, the soft propeller is actuated at the base by a simple rotatory motor and it naturally adapts to the action of the surrounding fluid. The propeller's helical shape, providing the final thrust, is the simple consequence of the elastic behaviour of the material's module, i.e. its embodied intelligence. Moreover, being soft, the module is particularly suitable for navigating in cluttered environment or to monitor the delicate marine environment with a reduced risk of causing damages [18].

In this paper, we further investigate this family of soft propellers and their behaviour, towards improved swimming performances. Since the behaviour of the propeller is bounded with its shape and material, the optimization of these parameters appears as a fundamental step in the design process. This is allowed by the presence of an accurate, yet simple, theoretical model. The new prototype is then fabricated through the definition and characterization of a composite material that is able to

provide the required optimal stiffness. A simple robotic device is then employed to test the swimming capabilities of the new improved design, which are compared with those obtained with the previous one. The elongated shape that resulted from this research paths the way to the definition of a multi-functional module, which is able to provide both locomotive and grasping capabilities.

The remaining parts of the paper are organized as follows. In Section II, the different components of the optimization process are defined. These include the design parameters, their boundaries and the definition of the system dynamics providing the objective function that should be maximised, which is its swimming speed. In Section III the numerical optimization and its results are presented, while in Section IV the optimal prototype is fabricated. The results are validated designing and fabricating a robotic prototype in Section V, where the performances are compared against the one provided by the previous design. Finally, in Section VI the conclusions and a discussion on the future prospective of the research are presented.

II. OPTIMIZATION COMPONENTS

The first prototype of the bio-inspired soft flagellar propeller was presented in [17]. It combines a soft elongated conical part, the *filament*, and a pre-curved cylindrical part, the *hook*, which is connected to a continuously rotating motor. Through the *hook*, the rotation of the motor is transmitted to the *filament*, which, interacting with the surrounding fluid, takes on an helical shape providing a propulsive thrust. The main purpose of the present paper is the optimization of this first prototype towards higher values of the generated thrust, to finally achieve improved locomotive (swimming) performances. This process requires, first of all, the depiction of the design parameters that most affect the overall behaviour of the propeller, their lower and upper boundaries and finally the identification of the objective and constraint functions.

A. Design Parameters

In [17] three different silicones were used to fabricate the soft modules, while a rigid one was 3D-printed using ABS. The experimental trials, corroborated by the theoretical predictions, proved that the soft module's performances are directly proportional with the stiffness of the material: the stiffer the silicone, the higher the thrust that the propeller provides. On the other end, a thrust reversal is observed when going from a soft to a rigid propeller, which provides a backward thrust, pulling the module instead of pushing it forward. This phenomenon can be explained considering that the propulsive thrust is generated by the helical shape taken by the propeller when interacting with the surrounding fluid. Being the module deformable, the angle of attack between the fluid and the module varies along its length. This results in a variation of the direction of the lift forces along the *filament*, whose sum finally generates the propulsive thrust. From these considerations, it is possible to conclude that the performances of the propeller are strictly related to the stiffness of the material, but also to its geometry. Finally, it was also observed that the swimming speed increases with the rotational

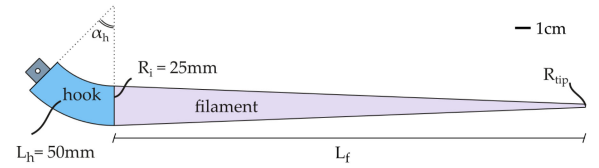


Fig. 2. Schematics of the soft propeller dimensions and the geometric design parameters. In particular, while the *hook's* length L_h and radius R_i are not modified with respect to the previous design, the *filament's* length L_f , the tip radius R_{tip} and the pre-curvature of the *hook* α_h are among the design parameters of the optimization process.

speed of the actuating motor. In conclusion, the main properties that affect the performance of the module, which are considered as the design parameters in the optimization process, are:

- 1) the geometry of the filament: its length L_f and cross section (represented here by the radius at the tip R_{tip});
- 2) the hook's pre-curvature angle α_h ;
- 3) the stiffness of the filament, which, for a linear-elastic material, is represented by the Young's Modulus E_f ;
- 4) the rotational speed of the actuating motor ω .

Since the *hook* is designed to transmit the motor's rotation to the filament and, through its pre-curvature, to define the direction of the thrust, its length and radius are not varied in the optimization and it is also assumed to be rigid. The dimensions of the hook and the geometric design parameters are summarized in Fig. 2 .

B. Dynamics of the System and Objective Function

For a given set of design parameters, the steady-state swimming speed is obtained solving the dynamics of the system, which thus represent the objective function of the optimization process. The mechanics of the considered hybrid rigid/soft system is described through the Geometric Variable-Strain (GVS) approach presented in [19] in statics and in [20] in dynamics. In particular, this approach has been recently implemented in SoroSim, a MatLab Toolbox for the modeling of general soft-rigid systems [21], which is employed here for the simulations. In this Section we present the main components of the dynamical description of the soft propeller. For more details, the reader is referred to the above mentioned works.

Following the Cosserat rod description, the configuration of a soft body is defined by a vector $\mathbf{r}(X, t) \in \mathbb{R}^3$, representing the position of the rod's mid-line, and a relative reference frame whose orientation is given by a rotation matrix $\mathbf{R}(X, t) \in SO(3)$. Both the mid-line and the orientation matrix are defined as functions of a curvilinear abscissa $X \in [0, L]$ where L is the length of the soft body. In this way, the configuration of the soft body with respect to the spatial frame is defined as a curve $\mathbf{g}(\cdot, t) : X \in [0, L] \mapsto \mathbf{g}(X, t) \in SE(3)$, given by:

$$\mathbf{g}(X, t) = \begin{pmatrix} \mathbf{R}(X, t) & \mathbf{r}(X, t) \\ \mathbf{0}^T & 1 \end{pmatrix} \quad (1)$$

Taking the partial derivatives of (1) with respect to space $(\cdot)'$ and time (\cdot) yields:

$$\mathbf{g}'(X) = \widehat{\mathbf{g}}\boldsymbol{\xi}(X), \quad \dot{\mathbf{g}}(X) = \widehat{\mathbf{g}}\boldsymbol{\eta}(X), \quad (2)$$

where $\xi(X)$ and $\eta(X)$ are, respectively, the strain twist and the velocity twist of the cross-section in the local frame. The equality of mixed partial derivatives of (1) leads to

$$\frac{\partial}{\partial t} \mathbf{g}' = \frac{\partial}{\partial X} \dot{\mathbf{g}} \Rightarrow \boldsymbol{\eta}' = \dot{\boldsymbol{\xi}} - \text{ad}_{\boldsymbol{\xi}} \boldsymbol{\eta}, \quad (3)$$

where ad is the adjoint operator of $SE(3)$. The integration in space of equations (2)₁ and (3) yields:

$$\mathbf{g}(X) = \exp(\widehat{\boldsymbol{\Omega}}(X)), \text{ and} \quad (4)$$

$$\boldsymbol{\eta}(X) = \text{Ad}_{\mathbf{g}(X)}^{-1} \int_0^X \text{Ad}_{\mathbf{g}} \dot{\boldsymbol{\xi}} ds, \quad (5)$$

where $\widehat{\boldsymbol{\Omega}}$ is the Magnus expansion of the field $\widehat{\boldsymbol{\xi}}$, \exp and Ad are the exponential and adjoint maps of $SE(3)$ [22].

Finally, in the GVS approach the configuration space is parametrized by the rod's strain fields, which are discretized on a truncated basis of strain functions:

$$\boldsymbol{\xi}(X) = \boldsymbol{\Phi}_{\xi}(X) \mathbf{q} + \boldsymbol{\xi}^*(X), \quad (6)$$

where $\boldsymbol{\Phi}_{\xi}(X) \in \mathbb{R}^{6 \times n}$ is a matrix function whose columns form the basis for the strain field, while $\mathbf{q} \in \mathbb{R}^n$ are the generalized coordinates, where n is the number of DoF. Finally, $\boldsymbol{\xi}^*(X)$ is the reference strain twist computed at the stress-free reference configuration $\mathbf{g}^*(X)$. Thus, the coefficients of the strains stand for the generalized coordinates of a set of homogeneous transformations along the soft robot, similar to the joint transformations for rigid ones [23], which can be obtained setting $X = L = 1$.

The recursive integration of (5) to all the bodies of the hybrid system yields to the definition of the geometric Jacobian $\mathbf{J}(\mathbf{q}, X) \in \mathbb{R}^{6 \times n}$, providing the relationship between the generalized coordinate vector \mathbf{q} and the body velocity twist $\boldsymbol{\eta}$:

$$\boldsymbol{\eta}(X) = \mathbf{J}(\mathbf{q}, X) \dot{\mathbf{q}}. \quad (7)$$

Through application of the principle of virtual work, this (relative) strain parametrization produces a highly reduced set of ODEs in the classical Lagrangian form:

$$\mathbf{M}(\mathbf{q}) \ddot{\mathbf{q}} + \mathbf{C}(\mathbf{q}, \dot{\mathbf{q}}) \dot{\mathbf{q}} + \mathbf{K} \mathbf{q} = \boldsymbol{\tau} + \mathbf{F}(\mathbf{q}, \dot{\mathbf{q}}), \quad (8)$$

where $\mathbf{M}(\mathbf{q})$ is the generalized mass matrix, $\mathbf{C}(\mathbf{q}, \dot{\mathbf{q}})$ is the generalized Coriolis matrix, \mathbf{K} is the generalized stiffness matrix, $\boldsymbol{\tau}$ is generalized actuation vector and finally $\mathbf{F}(\mathbf{q}, \dot{\mathbf{q}})$ is the vector of the generalized external forces. The action of the fluid, generating the propulsive thrust, is represented by the drag and lift forces contained in the vector $\mathbf{F}(\mathbf{q}, \dot{\mathbf{q}})$, while an added mass term, modeling the volume of fluid accelerated around the body, is combined with the generalized mass matrix. For more details on the hydro-dynamical modeling of the system, the reader is referred to [17].

The different components of the propeller are modeled as follows:

- 1) the canister containing the motor is represented by a prismatic joint;
- 2) the motor's shaft is modeled as an actuated revolute joint;
- 3) the *hook* is modeled as a rigid body characterized by the geometry presented in Section II-A;

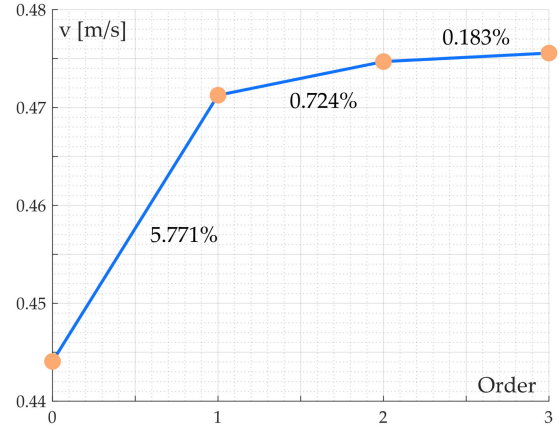


Fig. 3. Steady state velocities obtained at varying the order of the strain basis, for $L_f = 300 \text{ mm}$, $R_{tip} = 1 \text{ mm}$, $\alpha_h = 70^\circ$, $E = 8.5 \text{ MPa}$ and $\omega = 15 \text{ rd/s}$. The indicated percentages represent the increment in the steady state velocity that is obtained at increasing the order of polynomials employed as strain basis. In particular, going from quadratic (2nd order) to cubic (3rd order) polynomials, this difference is only 0.183%, and, accordingly, all the following simulations are performed using cubic polynomials.

- 4) the *filament* is modeled as an inextensible Kirchhoff-Love rod, whose DoF are the torsion about the out-of-plane axis and the bending about the other two axes.

In particular, polynomial functions are used as strain basis $\boldsymbol{\Phi}_{\xi}$ to model the *filament's* DoF in (6). The order of these polynomials is obtained from stand-alone simulations that are performed at increasing its value. These simulations are performed considering different module's geometries and material, and at varying the motor's speed. Fig. 3 presents the swimming speeds that are obtained employing 0, 1st, 2nd and 3rd order polynomials when simulating a soft propeller having $L_f = 300 \text{ mm}$, $R_{tip} = 1 \text{ mm}$, $\alpha_h = 70^\circ$, $E = 8.5 \text{ MPa}$ and for $\omega = 15 \text{ rd/s}$. In particular, going from a constant (0 order polynomial) to a linear (1st order) strain, the simulation provides a 5.771% increment in the steady state velocity. This discrepancy in the results is not observed when going from quadratic (2nd order) to cubic (3rd order) polynomials, and the latter are thus employed in all the following simulations.

C. Constraints, Lower and Upper Boundaries

The experimental set-up and the machines employed to fabricate the prototype determine the optimization constraints and the upper (and lower) boundaries of the design parameters. In particular, in the present paper the propeller is actuated by a high-power 6 V brushed DC motor having 47 : 1 gear ratio and a 0.89 Nm extrapolated stall torque. In order to avoid stalling or overloading, we considered a maximum torque $\tau_c = 0.5 \text{ Nm}$, which constitutes an inequality constraint to the optimization problem, $\tau \leq \tau_c$. It should be noted that the torque generated by the propeller for a fixed set of design parameters is also provided solving the the dynamics of the system, presented in Section II-B. In other words, the objective and the (inequality) constraint functions in the optimization process are obtained from the same algorithm and they are both provided by the simulations performed in SoroSim.

TABLE I
DESIGN PARAMETERS BOUNDARIES

	L_f [mm]	R_{tip} [mm]	α_h [°]	ω [rad/s]	E_f [Pa]
Lower b.	300	1	0	3	$1379 \cdot 10^3$
Upper b.	700	50	90	22	$1681 \cdot 10^6$

The motor can provide a maximum rotating speed $\omega_{max} = 22 \text{ rd/s}$, which is thus considered as the upper boundary value for ω . With regards to the boundaries of the filament's geometrical parameters, these are mostly defined by the limitations resulting from the fabrication process. In particular, the soft propeller is obtained using an ad-hoc Teflon mold, fabricated using a CNC machine, where the silicone is injected after being vacuum degassed. In particular, the dimension of the CNC machine that is used to fabricate the mold provided the maximum length of the filament $L_{f,max} = 700 \text{ mm}$, while the maximum tip radius is set to be equal to twice the value of the cone's basis $R_{tip,max} = 50 \text{ mm}$. With regards to the filament's stiffness, we considered a maximum value of the Young's Modulus corresponding to ABS (i.e. a rigid propeller), $E_{f,max} = 1681 \cdot 10^6 \text{ Pa}$.

With regards to the lower boundaries of the parameters, these are set equal to those employed in the previous design and set-up. In particular, the lower limit for Young's Modulus is fixed to $E_{f,min} = 1378.95 \cdot 10^3 \text{ Pa}$, corresponding to the stiffest silicone considered in [17] (Smooth-SilTM940). Finally, the design parameters with the corresponding lower and upper boundaries that were considered in the optimization problem are summarized in Table I.

III. NUMERICAL OPTIMIZATION AND RESULTS

From the previous Sections, we can conclude that the main components of the optimization process are:

- 1) *Design Parameters*: $\mathbf{x} = [L_f, R_{tip}, \alpha_h, \omega, E_f]$;
- 2) *Objective function*: Providing the steady state swimming speed v , which is given by the dynamics simulation performed in SoroSim;
- 3) *Inequality Constraint*: $\tau \leq \tau_c = 0.5Nm$, which is also given by the dynamics simulations in SoroSim;
- 4) *Lower and Upper Boundaries*: Of the design parameters.

The optimization is performed using the Global Optimization Toolbox available in MATLAB®. The Toolbox solver includes different optimization methods, which are mostly varying in the way they compute the search direction at each iteration, [24]. There are *derivative-based* methods, which, as the name suggests, compute or approximate the gradients of the objective and the constraint functions to obtain the optimal point search direction. Clearly, these methods require that the same functions are differentiable, which is the case of the GVS approach employed in the present paper. While representing the canonical optimization methods, *derivative-based* approaches can also be computationally expensive, especially when dealing with highly non-linear problems as the one considered here. One other family of methods that are available in the Global Optimization Toolbox are the *direct research* ones. These are also called derivative-free methods, since the search direction is obtained

employing only the functions values, and not their gradients. Finally, *nature inspired* methods, such as genetic algorithms, should be preferred when dealing with large sets of design parameters or when the involved functions are not differentiable. For all these reasons, *direct research* methods appear as the most suitable for the problem investigated here. Among them, *Pattern Search* is one of the most popular solver available in the MATLAB®Global Optimization Toolbox. *Pattern Search* is a family of uni-variate search methods, where the objective function is minimized with respect to one variable at a time. They consist in two main steps: 1) the exploratory search, where the moving directions of each variables are investigated from a starting point; 2) the pattern search, where the solver performs the step, moving all the variables along the directions that were estimated, and the objective and the constraint functions are obtained.

It should be noted that *Pattern Search* provides the local minima of the objective function, while the considered optimization problem seeks for the global maximum steady state velocity. For this reason, the problem is formulated to find the minimum of the negative of the speed and the optimization is run multiple times, at varying starting points (initial guesses). These are randomly picked within the range defined by the upper and lower boundaries of the design parameters presented in Table I. Once the initial guess is obtained, a first iteration is performed to check the inequality constraint and, if this is not preserved, an other set of initial parameters is randomly obtained. The other main properties of the considered optimization problem are summarized as follows.

- 1) It can be proved that the rate of convergence of the solver is reduced if the condition number of the Hessian matrices of the objective and constraint functions is close to unity. Since the condition number is given by the ratio between the biggest and the smallest eigenvalues of the matrix, it is particularly important that the design variables are defined in order to have comparable sizes. In other words, all the design variables are scaled with respect to some references quantities, in order to be represented by numbers having the same order of magnitudes. In particular, the following reference quantities were employed: $L_{f,0} = 1 \text{ m}$, $R_{tip,0} = 10^{-2} \text{ m}$, $\alpha_0 = 45^\circ$, $\omega_0 = 10 \text{ rd/s}$, $E_{f,0} = 10^7 \text{ Pa}$.
- 2) The stopping criteria of the solver are set by the employed tolerances. In particular, `FunctionTolerance` sets the minimum change of the objective function between the iterations, while `MeshTolerance` defines the minimum size of the mesh that the solver employs. Both tolerances are set equal to 10^{-5} . Finally, the initial mesh size `InitialMeshSize` is set to 10^{-2} .
- 3) As previously explained, in the considered problem both the objective and the (inequality) constraint functions are obtained from the simulations performed with SoroSim Toolbox. In order to avoid un-necessary iterations that would require to solve the dynamics of the system twice at each step, a nested subroutine was employed. Finally, the *Parallelization Toolbox* was used to speed up the process.

In total, 60 optimizations were performed at varying the problem's initial guess, resulting in 60 different optimal designs.

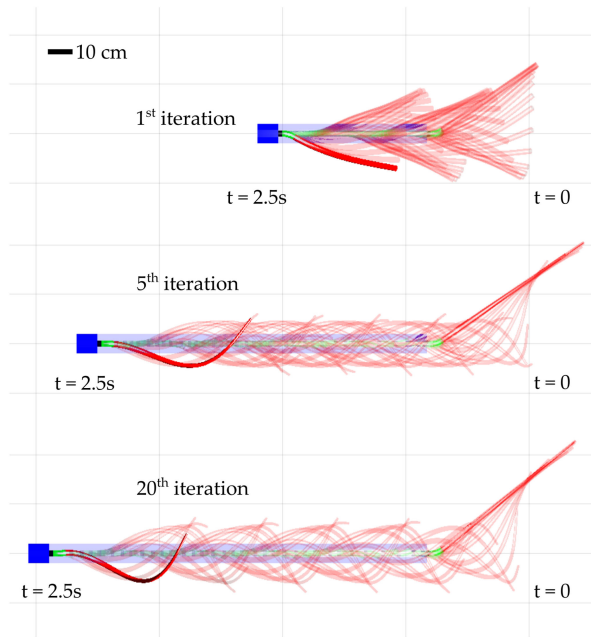


Fig. 4. Comparison between the results obtained at the 1st (top), 5th (middle) and 20th (bottom) iterations during one of the performed optimization process. In all three cases, the experiments are run for 2.5 s. It was observed that, on average, each optimization process required in total around 40 iterations, with an average total computation time of 5.40 hours (8.24 minutes per single iteration).

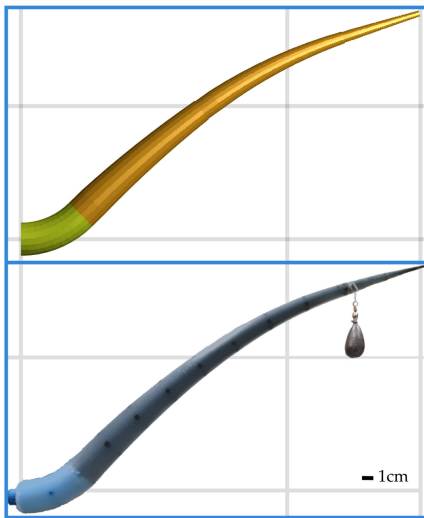


Fig. 5. Comparison between the simulated (top) and the experimental (bottom) deformed shapes during the static test performed to estimate the filament's stiffness. The comparison provided the composite material's stiffness $E_f = 7.9 \text{ MPa}$.

Fig. 4 presents the comparison of the results obtained, during one of the performed optimization, at the 1st, 5th and 20th iterations. It is possible to notice that after only 5 iterations the solver found a solution which is very similar to the optimal one, obtained at the 20th iteration. It was observed that, on average, each optimization process required in total around 40 iterations, with an average total computation time of 5.40 hours (8.24 minutes per single iteration).

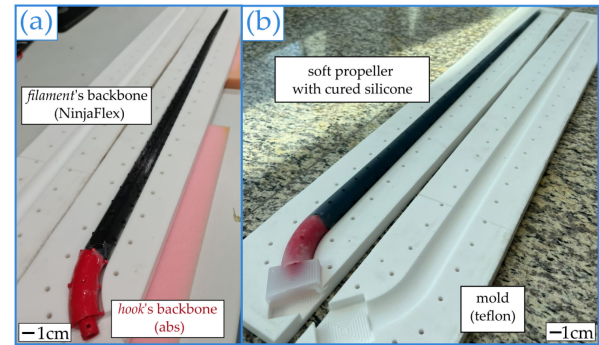


Fig. 6. Fabrication of the optimal soft propeller. (a) the rigid *hook* (red) and the *filament's* Ninjaflex (black) backbones inserted in the teflon mold before the silicone injection; (b) the soft propeller obtained after the curing of the silicone.

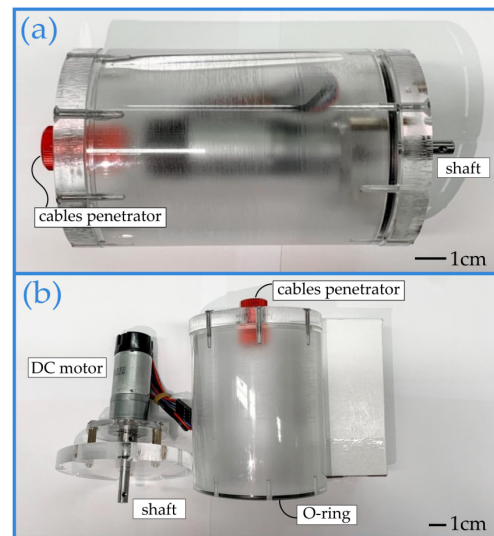


Fig. 7. The acrylic waterproof canister containing the DC motor, closed (a) and open (b). The canister is composed of a cylindrical body and two caps, passing the motor's shaft on one side and the cables, through a cable penetrator, on the other. The motor is supported by an acrylic base, connected to one cap through 4 spacers. O-rings are used to provide the required sealing.

TABLE II
OPTIMAL DESIGNS AND VELOCITIES

L_f [mm]	R_{tip} [mm]	α_h [°]	ω [rad/s]	E_f [MPa]	v m/s
700	5.65	42.30	14.4	7.4	0.683
700	5.41	41.40	14.6	7.6	0.680
700	4.84	40.05	14.4	9.1	0.673
700	4.67	39.60	14.4	9.4	0.671
700	4.55	39.15	14.5	9.6	0.668

Finally, Table II presents the 5 best solutions providing the highest swimming speeds.

From Table II it is possible to draw some conclusions on how the design parameters affect the overall behaviour of the propeller. In particular, it seems that higher lengths L_f provide higher speeds and this can be explained considering that an elongated *filament* provides an on-set of helical shapes, rather than a single one. Moreover, the optimal tip's radius R_{tip} appears to be around half the base's one at the *hook*. Indeed, higher values of the radius would result in higher drags, while on the other side

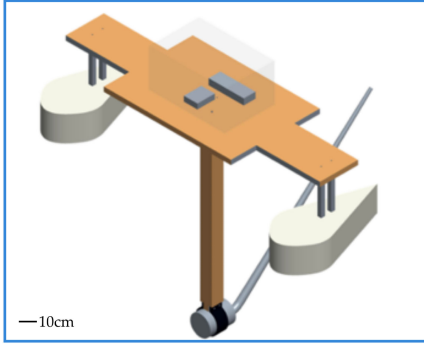


Fig. 8. Sketch of the hull structure employed to prevent the rotation of the canister. All the electronic components are placed in a box on top of the board.

a small tip radius reduces the tip's bending stiffness. With regards to the *hook* pre-curvature, when this is 0 a straight propeller is obtained and this does not provide any thrust. On the other end, a 90° *hook* also results in increased values of drag. Accordingly, the optimal angle appears to be close to 45° .

While the optimal geometric quantities L_f , R_{tip} , α_h and the motor's rotation ω present comparable values, a relatively large difference is observed in the value of the Young's Modulus E_f . This confirms once again that the material stiffness is, in fact, what mostly influence the propeller's behaviour. The propulsive thrust of the proposed device is generated by the on-set of helical waves, that are caused by the interaction between the soft propeller and the water (or, in other words, by the angle of attack between the cross section and the fluid flow). The propeller's stiffness is what mostly defines the deformed shape and, accordingly, it strongly affects the resultant propulsive thrust and the ratio between drag and lift forces. This was also observed in [17], where higher values of Young Modulus provided higher swimming speeds. On the other end, it was also observed, both in the simulations and in the experiments, that a rigid (underformed) propeller provides a negative thrust, pulling backward the device. This suggests that, for a given geometry and rotational speed, it is possible to obtain an optimal stiffness. Finally, it also seems that the Young Modulus is inversely proportional to the *hooke's* angle α_h and the tip's radius R_{tip} . These results suggest that the full understanding of the effect of the different parameters should be further investigated, possibly with a CFD software, which would also model the effect of the propeller on the fluid motion, which is not considered here. In this scenario, the results of our optimization process offer some first insights.

Finally, for the given tolerances, constraints and design boundaries, the optimization provided the global minimum to the considered problem, corresponding to the optimal design $[L_f, R_{tip}, \alpha_h, \omega, E] = [700 \text{ mm}, 5.65 \text{ mm}, 42.30^\circ, 14.4 \text{ rd/s}, 7.4 \cdot 10^6 \text{ Pa}]$.

IV. FABRICATION

Following the same approach presented in [17], the soft propeller is fabricated by injection molding. While the optimal

TABLE III
COMPOSITE MATERIAL COMPONENTS

Material		$E[\text{Pa}]$
Dragon Skin™ 50	50	$592 \cdot 10^3$
Ninjaflex		$17 \cdot 10^6$
Composite		$7.4 \cdot 10^6$

geometrical parameters (L_f , R_{tip} , α_h) define the mold specifications, the optimization resulted in a specific value of the Young's Modulus $E_f = 7.4 \text{ MPa}$ which does not correspond to the 100% Modulus of any available on-the-shelf silicone. A composite material should be designed in order to provide the required optimal stiffness. The main idea that is pursued in the present paper consists in fabricating a stiffer, yet flexible, backbone that can be inserted in the mold and incorporated inside the silicone. Thus, the investigated composite material is characterized by two components (phases): (1) a 3D-printed flexible backbone, made out of Ninjaflex; (2) the external silicone coating made with Dragon Skin™50 by Smooth-Sil. Both materials properties are summarized in Table III, where the final composite material's Young Modulus is also reported.

The dimensions of the backbone providing the required composite stiffness can be obtained using the rule of mixtures formula, a weighted mean that is often employed in material science to approximate composite materials properties. This approach relies on the assumption that a certain composite property is given by the volume-weighted-average of the phases properties. In particular, the rules of mixture is here applied to the bending stiffness of the propeller, which, under a linear-elastic assumption, is given by the product between the Young's Modulus E and the second moment of area of the cross section J :

$$(E_b J_b) \cdot V_b + (E_s J_s) \cdot V_s = (E_{comp} J_{comp}) \cdot V_{comp} \quad (9)$$

where the subscripts b , s and $comp$ refer to the backbone, the silicone and the composite materials, respectively. In particular, the Young Modulus are given in Table III, while the volume V_{comp} and the inertia J_{comp} of the final composite are given by the optimization results. It is then possible to define β as the ratio between the backbone's and the silicone's radius, which, assuming a conical backbone having the same cone angle of the external module, is constant along the length of the *filament*. The volumes V_s and V_b and the moments of inertia J_s and J_b can then be expressed as functions of β and, finally, (9) provides $\beta = 0.81$. The accuracy of the composite material characterization is experimentally validated on the previous propeller's design, characterized by $L_f = 300 \text{ mm}$, $R_{tip} = 2 \text{ mm}$ and $\alpha_h = 45^\circ$. The Ninjaflex backbone is 3D printed using a LulzBot Taz 6 3D printer, while the rigid hook is obtained employing an ABS backbone. The two backbones were interlocked and inserted inside a Teflon mold where, after being degassed in a vacuum chamber, the Dragon Skin™50 silicone is finally injected. The main benefit of using Teflon to fabricate the mold is represented by its low porosity that does not require the employment of any release agent, significantly easing the casting process. After 12 hours, the silicone is completely cured and the mold can be opened. The

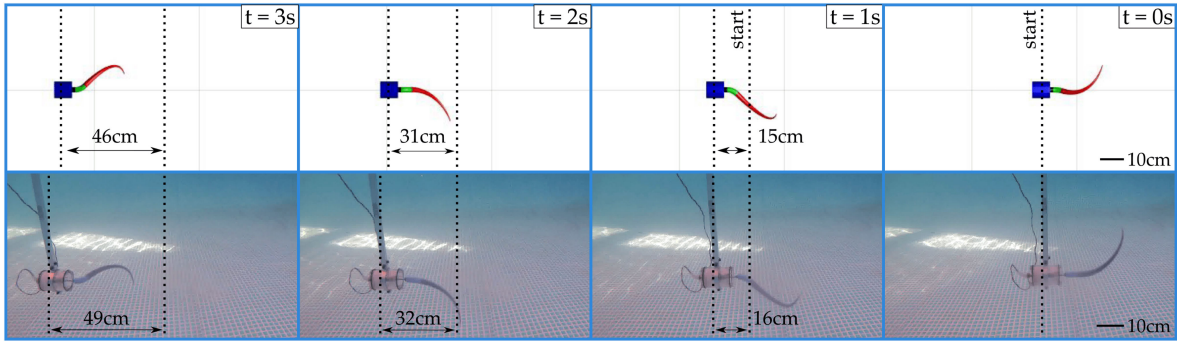


Fig. 9. Comparison between the experimental results and the theoretical predictions for the previous design. In 3 seconds, the simulations predict that the prototype travels for 0.46 m , and the average swimming speed is 0.154 m/s . A similar result is obtained from the experiments, where the prototype's average speed is 0.160 m/s . The complete videos are contained in the supplementary material.

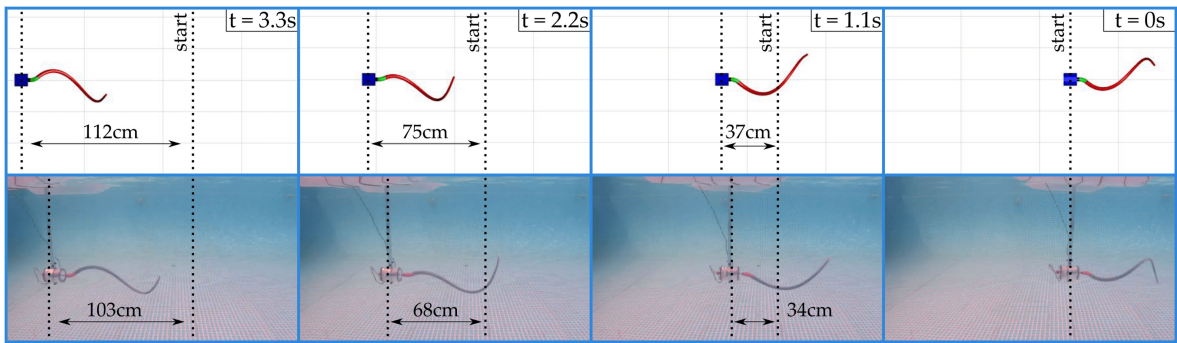


Fig. 10. Comparison between the experimental results and the theoretical predictions for the optimized design. In 3.3 seconds, the simulations predict that the prototype travels for 1.12 m , and the average swimming speed is 0.340 m/s . A similar result is obtained from the experiments, where the prototype's average speed is 0.311 m/s . The complete videos are contained in the supplementary material.

stiffness of the obtained material is estimated through a simple static experiment: the propeller is fixed in an upward position and some weights are applied in different points along the filament's length. The deformed shape is then compared with the one predicted by the numerical simulations for different values of E_f , Fig. 5. The Young Modulus providing the best matching between the simulated and the experimental deformed shapes is $E_f = 7.9\text{ MPa}$, corresponding to a 6% difference with respect to the one obtained from (9). This difference can be explained considering the porosity of the Ninjaflex backbone that partially absorbed the silicone, thus also requiring some silicone top ups during the first hours of the curing process.

The optimal propeller is finally fabricated employing the same injection molding procedure previously discussed. Pictures of the backbone, the mold and the final module are presented in Fig. 6. In order to prevent the retreat of the silicone caused by the porosity of the Ninjaflex material, the mold is designed to include a silicone reservoir on top.

V. EXPERIMENTAL TESTS

In order to validate the optimization results, an un-tethered prototype is designed and fabricated to perform a free swimming test. The soft propeller is connected to a stainless steel shaft and a waterproof acrylic canister is designed to contain the

motor, Fig. 7. A cable penetrator is used to provide a waterproof, high-pressure seal and to pass the motor's cable. O-Rings are inserted on both ends of the canister and on the motor's shaft to provide the required sealing. The rotational velocity of the motor is controlled via a microcontroller board based on ATmega328P (Arduino Uno Rev. 3), connected to an ESC board (45 A Brushed type) powered by a $7.4\text{ V }2\text{S}$ Lipo Battery. The DC motor has an integrated 48CPR quadrature encoder on the motor shaft, which provides 2248.86 counts per revolution of the gearbox's output shaft. A controller is implemented in the form of a velocity PI, employing the feedback from the encoder, with variable gain to compensate for cogging and static friction at very low speed, obtaining stable operation in the desired range of velocity. Finally, a Bluetooth Transceiver Module is used to wirelessly communicate to the microcontroller board from a portable device (e.g. laptop, smartphone), setting the desired rotational speed and receiving the measured error.

Employing a single propeller, particular attention should be paid to constrain the rotation of the canister that are caused by the motor's torque. Indeed, during a complete rotation of the motor, only two of the reaction forces provided by the propeller are not zero: the propulsive thrust and the out-of-plane torque. For this reason, a system of boat hull structures is employed. Through a clamp, the canister is held by a passive arm which,

on the water's surface, is connected to a wood board supported two polystyrene hull structures, Fig. 8. During the swimming of prototype, the submerged part of the hull structures naturally adapts to the motion, constraining the canister's rotation. Finally, all the electronic components required to control and power the motor are kept inside a box placed on the wood board.

A. Experimental Results

The free swimming of the single module robotic prototype is tested in a $5 \times 10 \text{ m}^2$ pool, 1.5 m deep. The experimental tests have been performed comparing the performances of the optimal soft module and the old-design module, both fabricated with the composite material from Section IV. In both cases the motor is run at the maximum speed that can be reached with the provided power. Snapshots from the videos taken during the experiments are presented in Figs. 9 and 10.

Thanks to the capability of the hull structure to constrain the canister rotations, a straight motion is obtained. The average swimming speed of the old design is $v = 0.160 \text{ m/s}$, while the optimal design speed $v = 0.311 \text{ m/s}$. Similar results are obtained from the simulations, which have been performed to include also the presence of the hull structure, represented by drag and lift forces acting on the canister. The previous design swimming speed predicted by the simulation is 0.154 m/s , while it is 0.340 m/s for the optimized design (3.75% and 9.32% errors, respectively). Finally, from the comparison of the experiments and the simulations presented in Figs. 9 and 10 it is possible notice the good agreement between the obtained deformed shapes.

VI. CONCLUSION

In this paper we presented the model-based design optimization and testing of a bio-inspired soft underwater propeller. Leveraging on the first results obtained in a previous work and on the power of an accurate theoretical tool, we were able to further investigate the propulsive mechanism of this new family of propeller and, finally, to design a new, improved, prototype. This is also characterized by a composite material whose elastic behaviour is predicted and tested through simple calculations and experiments. Finally, a robotic prototype has been fabricated to validate the accuracy of the theoretical predictions and to test the improved performances. In this way, we demonstrated how the Geometric Variable Strain (GVS) approach can be efficiently combined with other theoretical toolboxes to provide a model-based optimization, a topic which, at the moment, is only partially covered in literature (even though increasing in numbers). Moreover, since the GVS approach is able to model soft, rigid and hybrid soft-rigid robots, the same model-based optimization can be performed for a great number of underwater robots, including other bio-inspired designs characterized by different swimming strategies.

One of the main property of the optimal soft module is its elongated shape. This appears as particularly promising for the design of a multitasking module, providing both the locomotion of the vehicle and manipulations capabilities. A simple bending actuation, such as embedded tendon cables or pneumatic driven

chambers, can provide this soft elongated appendage with a curled shape that would perfectly fit a manipulation task. Once more, the embodied intelligence philosophy is pursued, where the employment of multiple soft modules would allow the caging of different objects, ranging in their shapes and sizes.

REFERENCES

- [1] M. Cianchetti, "Embodied intelligence in soft robotics through hardware multifunctionality," *Front. Robot. AI*, vol. 8, 2021, Art. no. 724056.
- [2] R. Pfeifer, M. Lungarella, and F. Iida, "Self-organization, embodiment, and biologically inspired robotics," *Science*, vol. 318, no. 5853, pp. 1088–1093, 2007.
- [3] G. Alici, "Softer is harder: What differentiates soft robotics from hard robotics?," *MRS Adv.*, vol. 3, no. 28, pp. 1557–1568, 2018.
- [4] C. Laschi, B. Mazzolai, and M. Cianchetti, "Soft robotics: Technologies and systems pushing the boundaries of robot abilities," *Sci. Robot.*, vol. 1 no. 1, 2016, Art. no. eaah3690.
- [5] A. D. Marchese, D. Onal Cagdas, and D. Rus, "Autonomous soft robotic fish capable of escape maneuvers using fluidic elastomer actuators," *Soft Robot.*, vol. 1, no. 1, pp. 75–87, Mar. 2014.
- [6] M. Calisti, G. Picardi, and C. Laschi, "Fundamentals of soft robot locomotion," *J. Roy. Soc. Interface*, vol. 14 no. 130, 2017, Art. no. 20170101.
- [7] F. Giorgio-Serchi, A. K. Lidtke, and G. D. Weymouth, "A soft aquatic actuator for unsteady peak power amplification," *IEEE/ASME Trans. Mechatronics*, vol. 23, no. 6, pp. 2968–2973, Dec. 2018.
- [8] F. Renda, F. Giorgio-Serchi, F. Boyer, C. Laschi, J. Dias, and L. Seneviratne, "A unified multi-soft-body dynamic model for underwater soft robots," *Int. J. Robot. Res.*, vol. 37, no. 6, pp. 648–666, 2018.
- [9] L. Manfredi et al., "A bioinspired autonomous swimming robot as a tool for studying goal-directed locomotion," *Biol. Cybern.*, vol. 107, no. 5, pp. 513–527, 2013.
- [10] S. J. Park et al., "Phototactic guidance of a tissue-engineered soft-robotic ray," *Science*, vol. 353, no. 6295, pp. 158–162, 2016.
- [11] T. Li et al., "Fast-moving soft electronic fish," *Sci. Adv.*, vol. 3, no. 4, 2017, Art. no. e1602045.
- [12] Z. J. Patterson, A. P. Sabelhaus, K. Chin, T. Hellebrekers, and C. Majidi, "An untethered brittle star-inspired soft robot for closed-loop underwater locomotion," in *Proc. IEEE/R SJ Int. Conf. Intell. Robots Syst. (IROS)*, 2020, pp. 8758–8764.
- [13] C. Armanini, C. Messer, A. T. Mathew, F. Boyer, C. Duriez, and F. Renda, "Soft robots modeling: A literature unwinding," 2021, *arXiv:2112.03645*.
- [14] T. Du et al., "Diffpd: Differentiable projective dynamics," *ACM Trans. Graph.*, vol. 41 no. 2, pp. 1–21, Nov. 2021.
- [15] D. M. Bodily, T. F. Allen, and M. D. Killpack, "Multi-objective design optimization of a soft, pneumatic robot," in *Proc. IEEE Int. Conf. Robot. Automat. (ICRA)*, 2017, pp. 1864–1871.
- [16] C. Duriez and B. Thor, "Soft robot modeling, simulation and control in real-time," in *Soft Robotics: Trends, Applications Challenges*. Cham, Switzerland: Springer, 2017, pp. 103–109.
- [17] C. Armanini, M. Farman, M. Calisti, F. Giorgio-Serchi, C. Stefanini, and F. Renda, "Flagellate underwater robotics at macroscale: Design, modeling, and characterization," *IEEE Trans. Robot.*, vol. 38, no. 2, pp. 731–747, Apr. 2022.
- [18] K. C. Galloway et al., "Soft robotic grippers for biological sampling on deep reefs," *Soft Robot.*, vol. 3, pp. 23–33, 2016.
- [19] F. Renda, C. Armanini, V. Lebastard, F. Candelier, and F. Boyer, "A geometric variable-strain approach for static modeling of soft manipulators with tendon and fluidic actuation," *IEEE Robot. Automat. Lett.*, vol. 5, no. 3, pp. 4006–4013, Jul. 2020.
- [20] F. Boyer, V. Lebastard, F. Candelier, and F. Renda, "Dynamics of continuum and soft robots: A strain parameterization based approach," *IEEE Trans. Robot.*, vol. 37, no. 3, pp. 847–863, Jun. 2021.
- [21] A. T. Mathew, I. Ben Hmida, C. Armanini, F. Boyer, and F. Renda, "Sorosim: A matlab toolbox for soft robotics based on the geometric variable-strain approach," 2021, *arXiv:2107.05494*.
- [22] J. M. Selig, *Geometric Fundamentals of Robotics. Monographs in Computer Science*. New York, NY, USA: Springer, 2007.
- [23] R. M. Murray, Z. Li, and S. S. Sastry, *A Mathematical Introduction to Robotic Manipulation*. Boca Raton, FL, USA: Taylor & Francis, 1994.
- [24] J. S. Arora, *Introduction to Optimum Design*. Boston, MA, USA: Academic Press, 2017.